Universal quantum computation based on nanoelectromechanical systems

Motohiko Ezawa [1], Shun Yasunaga [2], Akio Higo [2], Tetsuya Iizuka [2], and Yoshio Mita [2]

[1] *Department of Applied Physics, The University of Tokyo, 7-3-1 Hongo, Tokyo 113-8656, Japan*
[2] *Department of Electrical Engineering, The University of Tokyo, 7-3-1 Hongo, Tokyo 113-8656, Japan*

We propose to use a buckled plate as a qubit, where a double-well potential is mechanically produced by pushing the plate from both sides. The right and left positions of the plate are assigned to be quantum states $|0\rangle$ and $|1\rangle$. The NOT gate is executed by changing the buckling force acting on the plate, while the Pauli-Z gate and the phase-shift gate are executed by applying an electric field. A two-qubit phase-shift gate is materialized with the use of an electrostatic potential. They constitute a set of universal quantum gates. We estimate the relaxation time and the coherence time. We also discuss the fidelity of each gate operation. An examination of sample parameters leads to a feasibility of a nano-electro-mechanical-system-based quantum computer.

I. INTRODUCTION

According to Moore's law, elements of integrated circuits become exponentially small as a function of year. The size will become the order of nanometers within 10 years, where quantum mechanical effects are inevitable. For example, the superposition of states and entanglement occur, which are absent in classical mechanics. It is impossible to decrease the size of elements smaller than 1 nm, which is a typical scale of atoms. This is the end of Moore's law. Quantum computation [1–3] is a candidate for "More than Moore," which resolves the limit of Moore's law. It gives an exponential speedup for some algorithms. The problem is how to materialize a qubit based on actual materials. Various proposals have been made such as superconductors [4], photonic systems [5], quantum dots [6], trapped ions [7], and nuclear magnetic resonance [8,9]. Nanoscale-skyrmion-based qubits [10,11] and meron-based qubits [12] have also been proposed.

A micro-electro-mechanical system (MEMS) is one of the basic elements in current technology [13–15]. It uses electrostatic energy to induce mechanical motions. If the size becomes of the order of nanometers, it is called a nano-electro-mechanical system (NEMS) [16,17]. It has been demonstrated [18–20] that quantum effects emerge in the oscillation modes of a cantilever, which are described by a quantum harmonic oscillator. Carbon nanotubes, DNAs, or biomolecules are used to compose elements in a NEMS. Quantum effects have also been observed for a buckled beam made of a carbon nanotube. Nanomechanical qubits have been proposed in this context [21–23].

The buckled plate has two stable positions. It can be used as a classical bit. It has been proposed that an Ising annealing

machine is executable by a series of buckled plates [24]. Its mechanism is based on the electrostatic potential inducing the Ising interaction between two adjacent plates.

A buckled plate would also reveal quantum effects when the displacement is sufficiently small. In this paper, we propose to use it as a quantum bit, which is well described by a double-well potential. We then propose how to construct a set of universal quantum gates based on a buckled plate MEMS, which consists of the phase-shift gate, the HADAMARD gate, and the CNOT gate. They are constructed by tuning the tension, applying an electric field, and voltage. A merit is that it is not necessary to use an external magnetic field.

This paper is composed as follows. In Sec. II, we consider a chain of buckled plates at regular intervals along a line. When their size is of the order of nanometers, the dynamics is described by a Schrödinger equation with a double-well potential for each plate. The qubit state $|0\rangle$ or $|1\rangle$ is assigned to the plate buckled to the right- or left-hand side. The system is 2^N-fold degenerate when there are N plates. Although they are degenerate, quantum tunneling is prohibited due to a large double-well potential barrier between the two states $|0\rangle$ and $|1\rangle$.

In Sec. III, we discuss how to perform quantum gate operations. First, we construct the $\sqrt{\text{NOT}}$ and the NOT gates. In the case of the NOT gate, for instance, we transform the qubit state $|0\rangle$ to $|1\rangle$ by changing the buckling force acting on the plate so as to transform the double-well potential to a single-well potential. Next, we construct the phase-shift and Pauli-Z gates, where we change the phases of the qubit states $|0\rangle$ and $|1\rangle$ by temporally controlling an applied field. Then, we discuss the Ising gate and the CNOT gate, which are two-qubit gates. Universal quantum computation is possible with the use of these gate operations.

In Sec. IV, we discuss how to read out the gate operations. In Sec. V, we estimate the relaxation time and the coherence time. We argue that it is possible to execute quantum gates 100 times for a sample with the Q factor $Q = 10^3$, and 10^4 times for a sample with $Q = 10^6$ under a reasonable assumption on
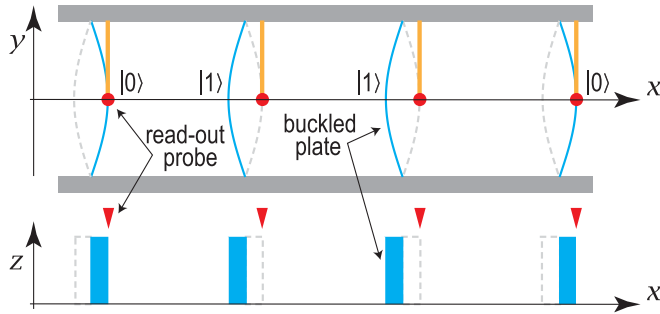
FIG. 1. A series of buckled plates, representing the bit state $|0110\rangle$. The position of each buckled plate is read out with the aid of a cantilever probe, indicated in red.

the sample parameters. In Sec. VI, we estimate the fidelity for each gate operation.

Section VII is devoted to discussions, where the feasibility of a NEMS-based quantum computer is addressed. Appendices are presented. We review how to derive the double-well potential for a buckled plate, where the parameters defining the double-well potential are explicitly fixed with the use of sample parameters. We also review how to estimate the relaxation time and the coherence time.

II. QUANTUM NEMS AND QUBITS

A. Quantum NEMS

The bistable structure of a buckled plate has been studied with a typical application to memories [24–26]. It was proposed [24] to use this buckled plate as the classical bit information 0 (1), when it is buckled rightward (leftward), as illustrated in Fig. 1.

We push a plate from both ends. The position along the x axis is determined to be $x = \pm a$ by minimizing the double-well potential [24,27] $V_{\mathrm{DW}}(x)$,

$$\mathcal{V}_{\mathrm{DW}}(x) = \lambda(x^2 - a^2)^2, \tag{1}$$

where explicit representations of λ and a in terms of the sample parameters are given in Appendix A. The buckled plate is an example of a MEMS (NEMS), when its size is of the order of micrometers (nanometers).

The dynamics of a buckled NEMS is described by the Schrödinger equation

$$i\hbar \frac{d}{dt}\psi(x,t) = H\psi(x,t), \tag{2}$$

where the Hamiltonian is

$$H = -\frac{\hbar^2}{2m}\frac{d^2}{dx^2} + \mathcal{V}_{\mathrm{DW}}(x), \tag{3}$$

together with the double-well potential (1).

It is straightforward to rewrite the Schrödinger equation and the Hamiltonian as

$$i\frac{d}{d\tau}\psi(X,\tau) = \tilde{H}\psi(X,\tau) \tag{4}$$

and

$$\tilde{H} = -\frac{1}{2}(d/dX)^2 + (X^2 - A^2)^2 \tag{5}$$

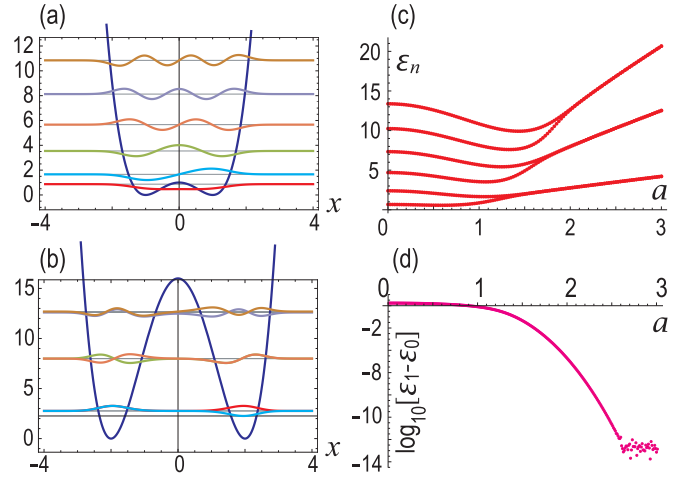FIG. 2. Wave functions and the energy spectrum by varying stress. (a) $a = x_{\mathrm{u}}$ and (b) $a = 2x_{\mathrm{u}}$. The horizontal axis is x in units of x_u, and the vertical axis is the energy in units of $\mathcal{E}_u$. The ground-state wave function is colored in red, while the first-excited state wave function is colored in cyan. (c) Energy spectrum as a function of a. (d) Logarithm plot of the energy difference between the ground state and the excited state.

in terms of the dimensionless time $\tau = t/t_{\mathrm{u}}$, the dimensionless parameters $X \equiv x/x_{\mathrm{u}}$ and $A \equiv a/x_{\mathrm{u}}$, and the dimensionless Hamiltonian $\tilde{H} = H/\mathcal{E}_{\mathrm{u}}$, where

$$t_{\mathrm{u}} = (m^2/\hbar\lambda)^{1/3}, \quad x_{\mathrm{u}} = \hbar^{1/3}/(m\lambda)^{1/6},$$
$$\mathcal{E}_{\mathrm{u}} = (\hbar^4\lambda/m^2)^{1/3} \tag{6}$$

give the units of time, space, and energy, respectively.

B. Qubits

We numerically determine the wave functions and the eigenenergies of the double-well system [28,29], which are shown in Fig. 2. They are those of the nondegenerate levels for small a ($a/x_{\mathrm{u}} \ll 1$) and those of twofold degenerate levels for large a ($a/x_{\mathrm{u}} \gg 1$). They are well described by those of the harmonic potential for large a.

We represent the qubit state $|0\rangle$ by the wave function $\psi_+(x)$ localized at $x = +a$ and the qubit state $|1\rangle$ by the wave function $\psi_-(x)$ localized at $x = -a$. Their degeneracy is resolved for $a \ll x_{\mathrm{u}}$, where the ground state is well described by the symmetric state $(\psi_+ + \psi_-)/\sqrt{2}$.

Actually, the twofold degeneracy is slightly broken for finite a. The energy difference between the ground state and the first-excited state is calculated. The $\log_{10}(\mathcal{E}_1 - \mathcal{E}_0)$ is plotted in Fig. 2(d). It is found that the energy difference is as tiny as $10^{-14}\mathcal{E}_{\mathrm{u}}$ at $a \approx 2.5x_{\mathrm{u}}$.

The potential is approximated by the harmonic potential,

$$\mathcal{V}_{\mathrm{DW}}(x) \simeq 4a^2\lambda(x \mp a)^2 + o[(x \mp a)^3], \tag{7}$$

in the vicinity of $x = \pm a$ with $a \gtrsim 2x_{\mathrm{u}}$, where the ground-state wave function is given by

$$\psi_\pm(x) = \left(\frac{m\omega}{\hbar\pi}\right)^{1/4} \exp\left[-\frac{m\omega}{2\hbar}(x \mp a)^2\right], \tag{8}$$

with the characteristic frequency $\omega = 2a\sqrt{2\lambda/m}$ and the ground-state energy $\mathcal{E}_0 = \hbar\omega/2$.

Since the two-qubit states $|0\rangle$ and $|1\rangle$ are degenerate, one may wonder if they are mixed by quantum tunneling. Then, the lifetime of a qubit state is too short. However, this is not the case because of a large double-well potential barrier. We estimate the tunneling rate as $\Gamma = e^{-2\varsigma}$ with $\varsigma = 3.1 \times 10^{10}$ for typical sample parameters in Appendix B.

When we align N buckled plates at regular intervals, we obtain the N-qubit system with 2^N-fold degenerate states $|s_1 s_2 \cdots s_N\rangle$, $s_i = 0, 1$. An instance of the four-qubit state $|0110\rangle$ is illustrated in Fig. 1.

C. Initialization

In quantum computation, we start with the state $|00\cdots0\rangle$, where all plates are buckled to the right-hand side. To generate this state, we start with the configuration where all plates are not buckled. Then, we gradually push all plates from both ends in the presence of an external electric field so that they are buckled toward the right-hand side to minimize the energy.

III. QUANTUM GATES

It is known that a set of the $\pi/4$ phase-shift gate, the HADAMARD gate, and the CNOT gate is enough for constructing any quantum circuits. It is known as the Solovay-Kitaev theorem of universal quantum computation [3,30,31]. We explicitly show that they are actually constructed in a buckled NEMS.

A. Construction of $\sqrt{\text{NOT}}$ and NOT gates

Our scenario reads as follows. Let us start from the state $|0\rangle$ at $a = a_0 \gtrsim 2x_\mathrm{u}$. For definiteness, we take $a_0 = 3x_\mathrm{u}$. We smoothly change the stable position a from a_0 to $a = 0$, where the double-well potential (1) is transformed to a single-well potential. Then, we smoothly change the position a back to the point a_0. More explicitly, by pushing the plate from both ends, we temporally control the stable position a according to a smooth function,

$$a(t) = \frac{a_0}{2}\left[\tanh\frac{t - t_2}{\mathcal{T}} - \tanh\frac{t - t_1}{\mathcal{T}} + 2\right], \quad (9)$$

with three parameters t_1, t_2, and $\mathcal{T}$. The resultant state need not be the state $|0\rangle$ or $|1\rangle$, but can be a superposition of $|0\rangle$ and $|1\rangle$ in general. We plot Eq. (9) in Fig. 4(a1) for the $\sqrt{\text{NOT}}$ gate, and in Fig. 4(b1) for the NOT gate.

We study the dynamics of the wave packet by numerically solving the Schrödinger equation (2) with a time-dependent Hamiltonian (3), where the double-well potential (1) is time dependent with the use of the time-dependent position (9).

We start from the initial state ψ_+ given by Eq. (8) localized at the right-hand side. In order to see the result of the gate operation, we focus on the state $\psi(x, t)$ after enough time of the gate operation at $t = t_3 \gg t_2$. We show the amplitudes $|\psi(\pm a_0, t_3)|$ and the phase shifts $\arg\psi(\pm a_0, t_3)$ as a function of t_2 in Figs. 3(a) and 3(b), respectively. They change significantly as a function of t_2. Indeed, $|\psi(\pm a_0, t_3)| = 0$ at
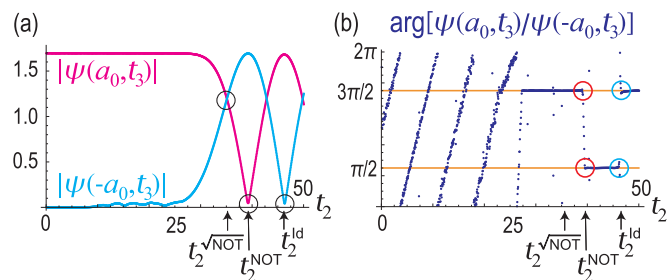

FIG. 3. (a) Absolute values $|\psi(\pm a_0, t_3)|$. They vanish at $t_2 = t_2^{\mathrm{NOT}}$ and $t_2 = t_2^{\mathrm{Id}}$, while they cross each other at $t_2 = t_2^{\sqrt{\mathrm{NOT}}}$. (b) The phase difference $\arg[\psi(a_0, t_3)/\psi(-a_0, t_3)]$. It has a gap at $t_2 = t_2^{\mathrm{NOT}}$ and $t_2 = t_2^{\mathrm{Id}}$. The horizontal axis is the parameter t_2 in units of t_u.

$t_2 = t_2^{\sqrt{\mathrm{NOT}}}$ and t_2^{NOT} as in Fig. 3(a), and the jumps occur in $\arg[\psi(a_0, t_3)/\psi(-a_0, t_3)]$ at these points as in Fig. 3(b).

1. $\sqrt{\text{NOT}}$ gate

We first construct the square-root NOT gate,

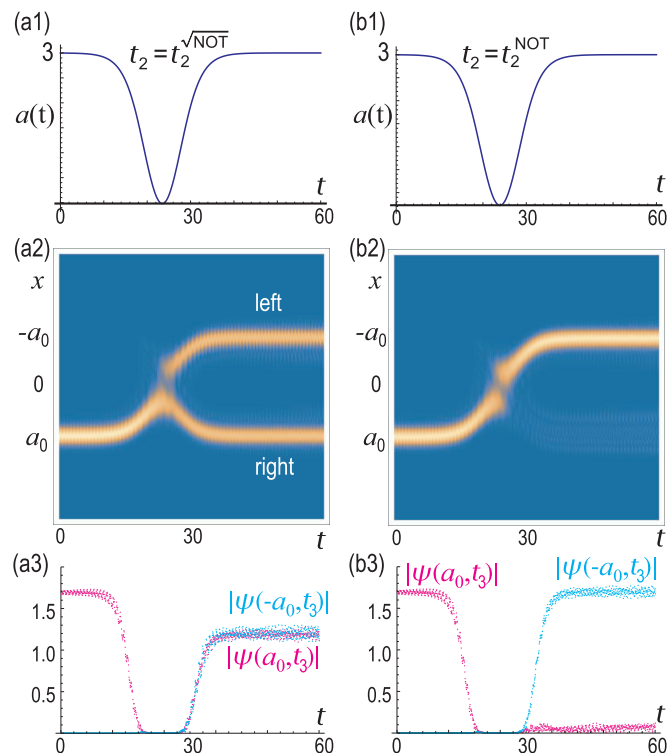$$U_{\sqrt{\mathrm{NOT}}}^{\pm} = \frac{1}{\sqrt{2}}(e^{i\pi/4}I_2 \pm e^{-i\pi/4}\sigma_x), \quad (10)$$

FIG. 4. (a) The $\sqrt{\text{NOT}}$ gate, where we have set $t_2^{\sqrt{\mathrm{NOT}}} = 27.02t_\mathrm{u}$. (b) The NOTgate, where we have set $t_2^{\mathrm{NOT}} = 28.87t_\mathrm{u}$. (a1),(b1) The time evolution of $a(t)$ given in Eq. (9) in units of x_u. (a2),(b2) The time evolution of the spatial profile of the absolute value of the wave function $\psi(x, t)$ starting from the localized state at the right-hand side. (a3),(b3) The time evolution of the wave functions $|\psi(\pm a_0, t)|$. We have set $a_0 = 3x_\mathrm{u}$, $t_1 = 20t_\mathrm{u}$, and $\mathcal{T} = 5t_\mathrm{u}$. The horizontal axis is the time ranging $0 < t < 60t_\mathrm{u}$.
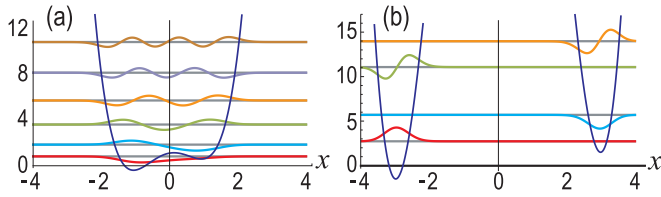
FIG. 5. Wave functions and the energy spectrum under electric field E_x. (a) $a = x_u$ and (b) $a = 3x_u$. The horizontal axis is x in units of x_u, and the vertical axis is the energy in units of E_u. The ground-state wave function is colored in red, while the first-excited state wave function is colored in cyan. We have set $qE_xa_0 = 0.5\mathcal{E}_u$.

which satisfies $(U^\pm_{\sqrt{\text{NOT}}})^2 = \pm\sigma_x$. We observe in Fig. 3(a) that the amplitude $|\psi(a_0, t)|$ at the initial position colored in magenta decreases for $t_2 > 26t_u$, and it becomes identical to $|\psi(-a_0)|$ colored in cyan at $t_2^{\sqrt{\text{NOT}}} = 27.02t_u$. This value of the parameter is special, where we study the time evolution of the spatial profile. The result is given in Fig. 4(a2), where the wave packet is split equally to the right and left positions. The time evolution of the amplitude at $x = \pm a_0$ is shown in Fig. 4(a3). We find that the wave function becomes stationary after the gate operation for $t \gtrsim 40t_u$. Precisely in the same way, the equal splitting occurs when we start from the initial state ψ_- given by Eq. (8) localized at the left-hand side. This gate operation at $t_2^{\sqrt{\text{NOT}}}$ is summarized as $U^\pm_{\sqrt{\text{NOT}}}$.

2. NOT gate

Next, we construct the NOT gate, $U_{\text{NOT}} \equiv \sigma_x$. We observe in Fig. 3(b) that the amplitude $|\psi(a_0, t)|$ at the initial position colored in magenta becomes zero at $t_2^{\text{NOT}} = 28.87t_u$. This value of the parameter is also special, where the wave packet moves to the left position as shown in Fig. 4(b2). The corresponding time evolution of the amplitude at $x = \pm a_0$ is shown in Fig. 4(b3). This is the NOT gate, σ_x. We find that the wave function becomes stationary after the gate operation for $t \gtrsim 40t_u$.

B. Construction of phase-shift and Pauli-Z gates

We proceed to construct the phase-shift gate. We apply an electric field along the x direction to the buckled plate, where the potential is given by qE_xx, with q being the electric charge stored in the plate. The potential and eigenfunctions under the electric field, $\mathcal{V}_{\text{DW}}(x) + qE_xx$, are shown in Fig. 5. We numerically evaluate the energy spectrum as a function

of the electric field, which is shown in Fig. 6(a). The energy difference between the ground state and the first-excited state monotonically increases with the increase of the electric field, as shown in Fig. 6(b). For $a_0 = 3x_u$, the energy spectrum changes linearly as a function of the electric field, as shown in Fig. 6(c). In the first-order perturbation theory, the energy is estimated as

$$\langle\psi_\pm|qE_xx|\psi_\pm\rangle = \pm qE_xa_0, \tag{11}$$

which is consistent with the numerical results shown in Fig. 6(c). This energy shift is represented by the effective Hamiltonian $H_{E_x} \equiv a_0qE_x\sigma_z$.

We have numerically evaluated the dynamics of the wave packet starting from the Gaussian distribution (8) under the temporally controlled electric field according to the formula

$$E_x(t) = \frac{E_0}{2}\left[\tanh\frac{t - t_1}{\mathcal{T}} - \tanh\frac{t - t_2}{\mathcal{T}}\right], \tag{12}$$

as shown in Fig. 7(a). The absolute value $|\psi(x, t)|$ does not change, but the phase is modulated as in Fig. 7(b) for the state $|\psi_+\rangle$. The phase modulation for the state $|\psi_-\rangle$ is precisely opposite that of the state $|\psi_+\rangle$. Hence, the result is summarized as the unitary operator,

$$U_Z(\theta) = \text{diag}(e^{-i\theta/2}, e^{i\theta/2}) = \exp\left[-\frac{i\theta}{2}\sigma_z\right], \tag{13}$$

where θ is determined as a function of t_2, as illustrated in Fig. 7(b). This is the phase-shift gate by angle θ.

1. $\pi/4$ phase-shift gate

The $\pi/4$ phase-shift gate $U_T \equiv \text{diag}(1, e^{i\pi/4})$ is realized by the z rotation (13) with the angle $\theta = \pi/4$ as $U_T = e^{-i\pi/8}U_Z(\frac{\pi}{4})$ up to the overall phase factor $e^{i\pi/8}$.

2. Pauli-Z gate

The Pauli-Z gate is realized by the z rotation with the angle π as $U_Z = -iU_Z(\pi)$ in a similar way.

C. The HADAMARD gate

The HADAMARD gate is defined by $U_H \equiv (\sigma_z + \sigma_x)/\sqrt{2}$. It is realized by a sequential application of the z rotation and the x rotation [32] as

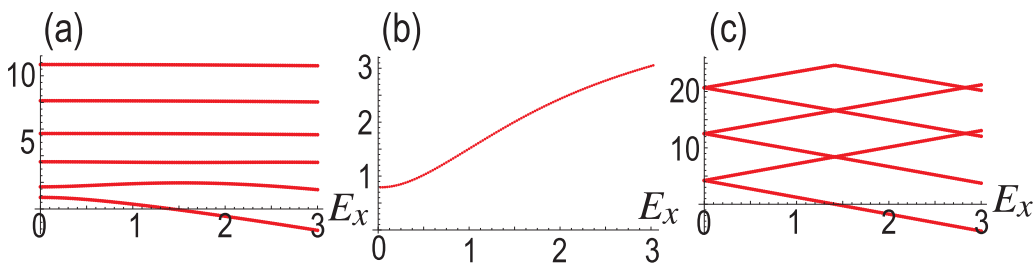$$U_H = -iU_ZU_{\text{NOT}}U_Z. \tag{14}$$

FIG. 6. Energy spectrum as a function of the applied electric field E_x in the case of (a) $a = x_u$ and (c) $a = 3x_u$. (b) The energy difference between the ground state and the first-excited state in the case of $a = x_u$. The horizontal axis is E_x in units of $\mathcal{E}_u/qa_0$.
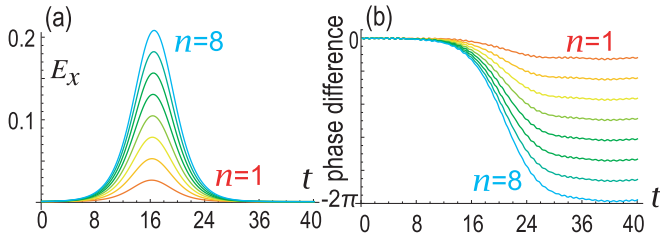
FIG. 7. (a) The time dependence of the applied electric field E_x according to (12). (b) The time evolution of the phase difference compared with the phase evolution without an electric field. The color indicates the time $t_2 = 20t_u + nt_{phase}$ ranging from $n = 1$ (red) to $n = 8$ (cyan), where $t_{phase} = 0.13t_u$. We have set $t_1 = 20t_u$. The horizontal axis is the time range $0 < t < 40t_u$. We have set $\mathcal{T} = 5t_u$.

D. Two-qubit phase-shift gate

Next, we construct two-qubit gates made of two buckled plates. In the parallel-plate NEMS, the capacitance between the plates x_1 and x_2 is well described by

$$C_{para}(x_1, x_2) = \frac{\varepsilon_0 S}{X_{cap} + x_1 - x_2}, \qquad (15)$$

where X_{cap} is the distance between the adjacent plates without buckling, S is the area of the plate, and ε_0 is the permittivity. The electrostatic potential is given by

$$U_{cap} = \frac{C_{para}(x_1, x_2)}{2} V_1^2, \qquad (16)$$

when we control the voltage V_1 between the plates.

We consider a set of two adjacent plates, where the potential energy is given by

$$\mathcal{V}(x_1, x_2) \equiv \mathcal{V}(x_1) + \mathcal{V}(x_2) + \frac{C_{para}(x_1, x_2)}{2} V_1^2. \qquad (17)$$

We show the potential in the $x_1 - x_2$ plane in Fig. 8. In the absence of the applied voltage $V_1 = 0$, there are fourfold degenerate bottoms at $u_1 = \pm a$ and $u_2 = \pm a$, as shown in Fig. 8(a), where the ground-state energy is $\hbar\omega$. Under the applied voltage, they are split as

$$\mathcal{V}(a, a) = \mathcal{V}(-a, -a) = \frac{\varepsilon_0 S}{X_{cap}} \frac{V_1^2}{2} \equiv E_0, \qquad (18)$$
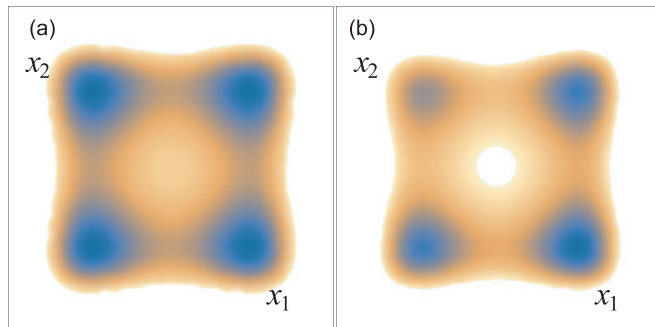

FIG. 8. Density plot of energy spectrum (17) in the $x_1 - x_2$ plane for (a) zero voltage $V_1 = 0$ and (b) nonzero voltage $\varepsilon_0 S V_1^2/2 = 100$. We have set $X_{cap} = 10x_u$ and $a = 2x_u$.

$$\mathcal{V}(a, -a) = \frac{\varepsilon_0 S}{X_{cap} + 2a} \frac{V_1^2}{2} \equiv E_+, \qquad (19)$$

$$\mathcal{V}(-a, a) = \frac{\varepsilon_0 S}{X_{cap} - 2a} \frac{V_1^2}{2} \equiv E_-. \qquad (20)$$

We plot the potential profile with nonzero voltage in Fig. 8(b). We assume that the plate distance X_{cap} is very large compared with the deviation a and obtain

$$\mathcal{E}_+ - \mathcal{E}_0 \simeq -\frac{a}{X_{cap}^2} \varepsilon_0 S V_1^2, \quad \mathcal{E}_- - \mathcal{E}_0 \simeq \frac{a}{X_{cap}^2} \varepsilon_0 S V_1^2. \qquad (21)$$

We assume that the plate distance X_{cap} is very large compared with the displacement a.

We start with the Gaussian state $\Psi_{\sigma_1\sigma_2}(x_1, x_2) \equiv \psi_{\sigma_1}(x_1)\psi_{\sigma_2}(x_2)$ with Eq. (8) localized at four points $x_1 = \sigma_1 a$ and $x_2 = \sigma_2 a$, where $\sigma_1 = \pm$, $\sigma_2 = \pm$. The absolute value of this wave function almost remains as it is for a potential at $a/x_u \gg 1$, but a phase shift occurs. The unitary evolution is given by

$$U(t) = \exp[-i(\mathcal{E}_0/\hbar + \omega)t] \qquad (22)$$

for $\sigma_1 = \sigma_2 = +$ and $\sigma_1 = \sigma_2 = -$,

$$U(t) = \exp[-i(\mathcal{E}_+/\hbar + \omega)t] \qquad (23)$$

for $\sigma_1 = +$ and $\sigma_2 = -$, and

$$U(t) = \exp[-i(\mathcal{E}_-/\hbar + \omega)t] \qquad (24)$$

for $\sigma_1 = -$ and $\sigma_2 = +$, where we have added the zero-point energy.

It corresponds to the two-qubit phase-shift gate

$$U_{2\text{-phase}}(t) = e^{-i\frac{E_0}{\hbar}t} \text{diag}(1, e^{-i\frac{E_X}{\hbar}t}, e^{i\frac{E_X}{\hbar}t}, 1), \qquad (25)$$

by identifying the qubit state $(|00\rangle, |01\rangle, |10\rangle, |11\rangle)^t = (|++\rangle, |+-\rangle, |-+\rangle, |--\rangle)^t$, where $\mathcal{E}_X = (\mathcal{E}_- - \mathcal{E}_+)/2$.

1. Ising gate

The Ising gate is defined by $U_{ZZ} \equiv \text{diag}(1, -1, -1, 1)$ and realized by setting $E_X t/\hbar = \pi$ in Eq. (25) up to the global phase $\exp[-i\mathcal{E}_0 t/\hbar]$.

2. CZ gate

The CONTROLLED-Z (CZ) gate is defined by $U_{CZ} = \text{diag}(1, 1, 1, -1)$. It is constructed by a sequential application of the Ising gate and the one-qubit phase-shift gates as [33]

$$U_{CZ} = e^{i\pi/4} U_Z\left(\frac{\pi}{2}\right) U_Z\left(\frac{\pi}{2}\right) U_{ZZ}. \qquad (26)$$

3. CNOT gate

The CNOT gate $U_{CNOT}^{1\to2}$ is defined by

$$U_{CNOT}^{1\to2} \equiv \begin{pmatrix} 1 & 0 & 0 & 0 \\ 0 & 1 & 0 & 0 \\ 0 & 0 & 0 & 1 \\ 0 & 0 & 1 & 0 \end{pmatrix}, \qquad (27)$$

where the first qubit is the controlled qubit and the second qubit is the target qubit. The CNOT is constructed by a sequen-

TABLE I. The Q factor, the relaxation time T_1, the coherence time T_2, and the number of the gate operations (Operation).

Q factor	T_1	T_2	Operation	Refs.
5×10^2	0.173 μs	0.170 μs	0.42	SiC [54]
4×10^3	1.38 μs	2.44 μs	3.45	Si [58] Gold [55]
10^4	3.46 μs	2.62 μs	6.55	Al [56]
10^5	34.6 μs	8.27 μs	20.7	SiN [57]
10^6	0.346 ms	10.5 μs	26.2	Al [40], SiN/Al [42]

tial application of the CZ gate (26) and the HADAMARD gate (14) as $U_{\text{CNOT}}^{1 \to 2} = U_{\text{H}}^{(2)} U_{\text{CZ}} U_{\text{H}}^{(2)}$.

IV. DECOHERENCE

We evaluate the relaxation time T_1 and the coherence time T_2. They are determined by the strength of the coupling between the qubit and bosonic modes due to the environment [34–38]. There are two contributions. One is the thermal fluctuation contributing to T_1 and T_2 and the other is the voltage fluctuation contributing only to T_2. As we review in Appendix C, they read

$$T_1 = \frac{2Q}{\omega_0(2\bar{n}_{\text{th}} + 1)}, \quad T_2 = \frac{4Q}{\omega_0(2\bar{n}_{\text{th}} + 1) + 8Q\gamma_z}, \quad (28)$$

where γ_z is a coupling constant between the voltage and the qubit, Q is the Q factor to be determined experimentally, ω_0 is the characteristic frequency, and $\bar{n}_{\text{th}}$ is the Bose distribution,

$$\bar{n}_{\text{th}}(\omega_0) = 1/(e^{\hbar\omega_0/k_{\text{B}}T} - 1). \quad (29)$$

As a typical characteristic frequency, let us take that of a carbon nanotube [39], $\omega_0 = 2\pi \times 327$ MHz.

At $T = 20$ mK, we have

$$T_1 = 1.38 \text{ μs}, \quad T_2 = 2.44 \text{ μs} \quad (30)$$

for $Q = 4 \times 10^3$ and

$$T_1 = 0.346 \text{ ms}, \quad T_2 = 10.5 \text{ μs} \quad (31)$$

for an ultrahigh quality factor $Q = 10^6$ as in Refs. [19,40–43]. We have used the value $\gamma_z = 23$ kHz. The results are comparable to the previous results on nanomechanical qubit $T_2 = 50$ μs $= 3$ kHz in Ref. [23]. We next evaluate the operation time in order to estimate how many times it is possible to execute quantum gate operations. The unit operation time is of the order of the time unit $t_{\text{u}} = (m^2/\hbar\lambda)^{1/3}$ given in Eq. (6). We obtain $t_{\text{u}} = (m^2/\hbar\lambda)^{1/3} = 10$ ns by assuming a typical mass of a carbon nanotube, $m = 10^{-21}$ kg, and the coefficient of the double-well potential (1), $\lambda = 3 \times 10^{15}$ kg/m^2 s^2, with a length of a NEMS $L_0 = 1$ μm and the buckled length $y_0 = 0.99$ μm. A typical gate operation time is $40t_{\text{u}} = 0.4$ μs, as shown in Fig. 4. It is shorter than the minimum value of the relaxation time T_1 and the coherence time T_2, and it is possible to execute quantum gates 3 times for a sample with $Q = 10^3$ and 26 times for a sample with $Q = 10^6$. See Appendix C for details.

We summarize the Q factor, the relaxation time T_1, the coherence time T_2, and the number of the gate operations in Table I.

V. CANTILEVER READOUT PROCESS

We discuss the readout process of the final positions of the buckled plates. For example, we prepare a detection cantilever probe for each buckled plate, as illustrated in Fig. 1. The probe detects the position with the aid of such as atomic force microscopy [44], capacitive interactions, mechanical or van der Waals interactions, resistive difference, or detecting electron field emission [45]. The merit is that it would be possible to construct an integrated circuit of the NEMS machine containing readout probes.

We explain the case to use an atomic force microscope (AFM) to detect the position of the buckled plate, as shown in Fig. 9. We attach a cantilever, where the atomic force is given by the Lennard-Jones potential,

$$U(r) = 4\varepsilon \left[\left(\frac{s}{r}\right)^{12} - \left(\frac{s}{r}\right)^6 \right], \quad (32)$$

with [46] $s = 2.4$ nm and $\varepsilon = 0.2$ eV $= 3.2 \times 10^{-20}$ J. The kinetic equation of the cantilever reads

$$m\frac{d^2x}{dt^2} = -\kappa\ell - \frac{dU}{dr}, \quad (33)$$

where r is the distance between the cantilever and the buckled plate, $r = \sqrt{(x-a)^2 + (\ell - \ell_0)^2}$, with x being the position of the buckled plate, $a = 0.127$ μm is the stable position of the buckled plate, ℓ is the position of the cantilever, and ℓ_0 is the vertical distance between the cantilever and the buckled plate.

The total potential of the cantilever is given by

$$U_{\text{canti}} = \frac{\kappa_0}{2}\ell^2 + 4\varepsilon \left[\left(\frac{s}{r}\right)^{12} - \left(\frac{s}{r}\right)^6 \right]. \quad (34)$$

The spring constant of the cantilever [47] is $\kappa_0 = 0.1$ kg/s^2. When the plate position is on the right side, we have $r = \ell_0 - \ell$. For $\ell_0 = 5$ nm, the stable position is determined as $\ell = 2.3$ nm. The position of the cantilever is detected by the Piezo effect, where the resistance is modified by the bending of the cantilever. The sensitivity of resistivity per unit displacement [47] is $\Delta R/(R\Delta\ell) \sim 6.3 \times 10^{-5}$ nm^{-1}, where $\Delta\ell$ is the displacement of the cantilever. The characteristic resistance of a cantilever is 2.5 kΩ [48]. The resistance change is 362 mΩ.

On the other hand, when the plate position is on the left side, we have $r = \sqrt{4a^2 + (\ell - \ell_0)^2}$. The stable position is $\ell = 0$ and there is no resistance change.

The ratio of the spring constant between the cantilever and the buckled plate is given by

$$\frac{\kappa_0}{\kappa} = \frac{0.1 \text{ kg/s}^2}{4.22 \times 10^3 \text{ kg/s}^2} = 0.24 \times 10^{-5}. \quad (35)$$

Hence, it is possible to read out the position of the buckled plate without affecting the position of the buckled plate. In addition, the moving directions of the buckled plate and the cantilever are diagonal, which assures the independence of the two motions. As a result, the position of the buckled plate can be read out by using a cantilever.

The resonant frequency [47] of the cantilever is 345 kHz. A typical readout time is estimated as $1/345$ kHz $= 2.90$ μs.
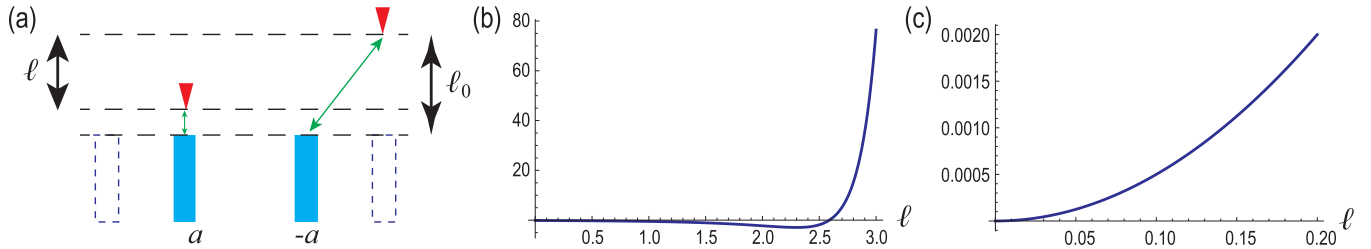
FIG. 9. (a) Illustration of the readout process. The red triangles represent the heads of cantilevers, the cyan rectangles represent buckled plates, and the green arrows represent the atomic force interaction. (b) Potential with the right-side position. (c) Potential with the left-side position. The horizontal axis is the position of the cantilever in units of nm. The vertical axis is the potential energy of the cantilever in units of $kg\, nm^2/s^2$.

It is comparable to the relaxation time $T_1 = 1.38$ μs with $Q = 4 \times 10^3$ given in (30) and much shorter than $T_1 = 0.346$ ms with $Q = 10^6$ given in (31). If we use an ultrahigh-frequency cantilever [49] with the resonant frequency 3.5 MHz, a typical readout is estimated as 0.286 μs, which is much faster than the relaxation time and the coherence time.

VI. FIDELITY

The fidelity for two wave functions ψ_ρ and ψ_σ is defined in general by

$$f(\sigma, \rho) = |\langle \psi_\rho | \psi_\sigma \rangle|^2, \tag{36}$$

where the wave function is given by $|\psi\rangle = \alpha |0\rangle + \beta |1\rangle$ for a single qubit. We estimate the fidelities of various gates by choosing σ as the numerically estimated wave function and ρ as the wave function of the ideal quantum gate. We also estimate the fidelity under noise for each gate operation.

A. Fidelity of the NOT gate

We calculate the fidelity of the NOT gate. An ideal gate process is

$$U_{\text{NOT}}|0\rangle = |1\rangle, \qquad U_{\text{NOT}}|1\rangle = |0\rangle. \tag{37}$$

We take an inner product between ideal result $|1\rangle$ and numerically obtained wave function $|\psi_{\text{numerical}}\rangle$ and it is estimated by

$$f_{\text{NOT}} \equiv |\langle \psi_{\text{numerical}} | 1 \rangle| = |\beta|. \tag{38}$$

We show the fidelity f_{NOT} as a function of the operation time t_2 in Fig. 10(a). We obtain $f_{\text{NOT}} = 0.9930 \pm 0.0018$.

Next, we introduce a noise in the gate operation process,

$$a(t) = (1 + \eta)\frac{a_0}{2}\left[\tanh\frac{t - t_2}{\mathcal{T}} - \tanh\frac{t - t_1}{\mathcal{T}} + 2\right], \tag{39}$$

where η represents a noise, which is a uniform random distribution ranging from $-\eta$ to η. We show the fidelity f_{NOT} as a function of the noise strength for the fixed time in Fig. 11(a). The error bar is estimated by the standard deviation of f_{NOT} in the range $50t_u \leqslant t \leqslant 60t_u$.

B. Fidelity of the $\sqrt{\text{NOT}}$ gate

The action of the $\sqrt{\text{NOT}}$ gate is given by

$$U_{\sqrt{\text{NOT}}}|0\rangle = \frac{e^{i\pi/4}}{\sqrt{2}}|0\rangle + \frac{e^{-i\pi/4}}{\sqrt{2}}|1\rangle. \tag{40}$$

The fidelity is calculated as

$$f_{\sqrt{\text{NOT}}} \equiv |\langle \psi | \psi_{\sqrt{\text{NOT}}} \rangle| = \left| \alpha \frac{e^{i\pi/4}}{\sqrt{2}} + \beta \frac{e^{-i\pi/4}}{\sqrt{2}} \right|, \tag{41}$$

for a single qubit, $|\psi\rangle = \alpha |0\rangle + \beta |1\rangle$. We show the fidelity $f_{\sqrt{\text{NOT}}}$ as a function of the operation time t_2 in Fig. 10(b). We obtain $f_{\sqrt{\text{NOT}}} = 0.9906 \pm 0.0026$.

We show the fidelity as a function of the noise strength for the fixed time in Fig. 11(b), where the noise is introduced in the same way as in the case of the NOT gate. The error bar is estimated by the standard deviation of $f_{\sqrt{\text{NOT}}}$ in the range $50t_u \leqslant t \leqslant 60t_u$.
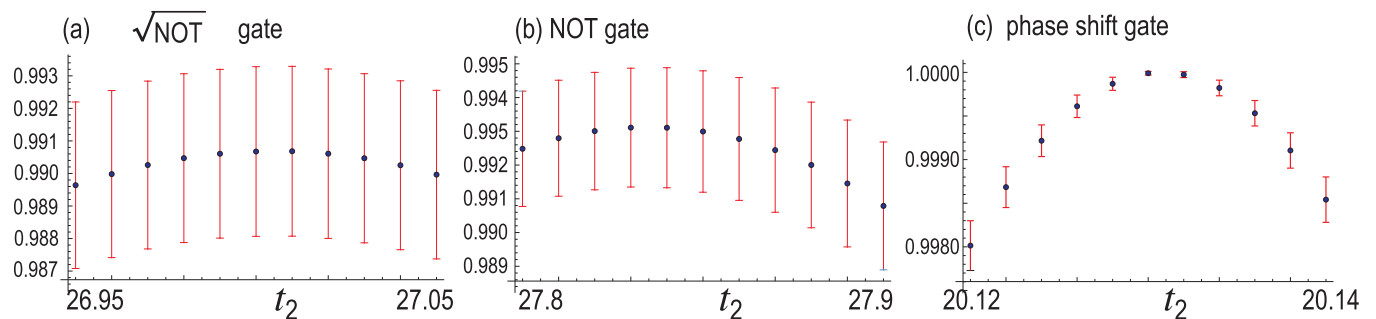

FIG. 10. Fidelity [Eq. (36)] as a function of operation time t_2 for (a) $\sqrt{\text{NOT}}$ gate, (b) NOT gate, and (c) phase-shift gate. We have set $t_1 = 20$, $a = 3x_u$, and $\mathcal{T} = 5t_u$. The error bar is estimated by the fluctuation in the range $0.5\mathcal{T} < t < \mathcal{T}$. The vertical axis is the fidelity.
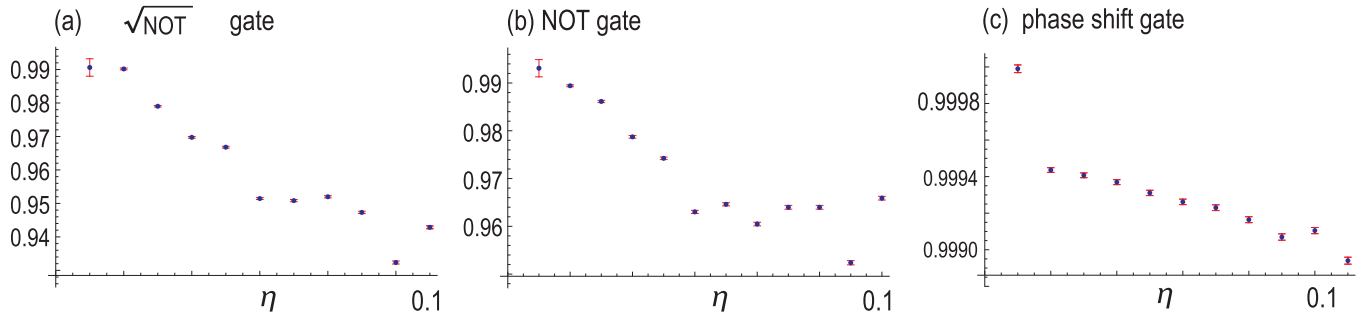
FIG. 11. Fidelity [Eq. (36)] as a function of noise strength η. (a) $\sqrt{\text{NOT}}$ gate, (b) NOT gate, and (c) phase-shift gate. We have set $t_1 = 20$, $a = 3x_u$, and $\mathcal{T} = 5t_u$. We have taken 100 times average of the randomness. The vertical axis is the fidelity.

C. Fidelity of the phase-shift gate

The action of the $\pi/4$ phase-shift gate is

$$U_T|0\rangle = |0\rangle, \quad U_T|1\rangle = e^{-i\pi/4}|1\rangle. \quad (42)$$

It is impossible to define the fidelity by the inner product for the phase-shift gate because it is always 1. Alternately, we estimate the fidelity by

$$f_{\text{phase}} \equiv \cos\left(\phi_{\text{numerical}} - \frac{\pi}{4}\right), \quad (43)$$

where $\phi_{\text{numerical}}$ is the numerically estimated phase. We show the fidelity f_{phase} as a function of the operation time t_2 in Fig. 10(c). Although there is a fluctuation in Fig. 7(b), the numerically estimated maximum fidelity f_{phase} is higher than 99.99.

The voltage fluctuation may occur during the gate process, which introduces a noise into the electric field,

$$E_x(t) = (1 + \eta)\frac{E_0}{2}\left[\tanh\frac{t - t_1}{\mathcal{T}} - \tanh\frac{t - t_2}{\mathcal{T}}\right]. \quad (44)$$

We show the fidelity as a function of the noise strength for the fixed time in Fig. 11(c). The error bar is estimated by the standard deviation of f_{phase} in the range $40t_u \leqslant t \leqslant 50t_u$.

VII. DISCUSSIONS

We have proposed a universal quantum computer based on a buckled NEMS lined up at regular intervals. We would like to discuss the difference between the previous proposals on nanomechanical qubits [21–23] and the present proposal on NEMS qubits. The previous works utilize a harmonic oscillation of a nanomechanical system, which leads to a bosonic mode. Then, they introduce anharmonicity by optomechanical coupling [21,22] or by coupling a quantum dot to a nanotube [23]. The major advance would be that strong anharmonicity is naturally introduced by buckling in the present proposal. In addition, we electrically control qubits and it would be possible to make an integrated system of many qubits with cantilever probes equipped.

Finally, we address the feasibility of the NEMS-based quantum computer by examining typical sample parameters [19]. The length of an element is of the order of ~ 1–$100\ \mu m$. The mass is of the order of $\sim 10^{-21}$–10^{-14} kg. The characteristic frequency is of the order of $\sim 1\ MHz$ to 1 GHz. Such a NEMS-based quantum computer would be realizable by improving the present technology.

APPENDIX A: BUCKLED PLATE MEMS

In this Appendix, we determine the parameters λ and a in the double-well potential (1) in terms of sample parameters. We consider a plate with length $2L_0$ and the spring constant κ placed along the y axis. The form of the buckled plate is determined by the Euler-Bernoulli equation [25],

$$\frac{d^4w}{dy^4} + m^2\frac{d^2w}{dy^2} = 0, \quad (A1)$$

with $m^2 \equiv P/EI$, where P is the axial load, E is Young's modulus of the beam material, and I is the second moment of area of the beam. In solving the Euler-Bernoulli equation for a clamped-clamped beam, we may use the fixed boundary condition or the free boundary condition.

First, we impose the fixed boundary condition, as shown in Fig. 12(a1), which reads

$$w(-y_0) = w(y_0) = 0, \quad \frac{dw}{dy}\bigg|_{y=-y_0} = \frac{dw}{dy}\bigg|_{y=y_0} = 0, \quad (A2)$$

where y_0 is the position of the supporting point along the y axis.

The lowest-energy solution is given by [50]

$$w = \frac{x}{2}\left(1 + \cos\frac{\pi y}{y_0}\right), \quad (A3)$$

where x is the position of the plate on the x axis. The length of the buckled plate is given by

$$L(x) = \int_{-y_0}^{y_0} dy\sqrt{1 + (dw/dy)^2}. \quad (A4)$$

It is calculated as

$$L(x) = \int_{-y_0}^{y_0} dy\sqrt{1 + \frac{\pi^2 x^2}{4y_0^2}\sin^2\frac{\pi y}{y_0}} = \frac{4y_0}{\pi}E\left(-i\frac{\pi x}{2y_0}\right), \quad (A5)$$
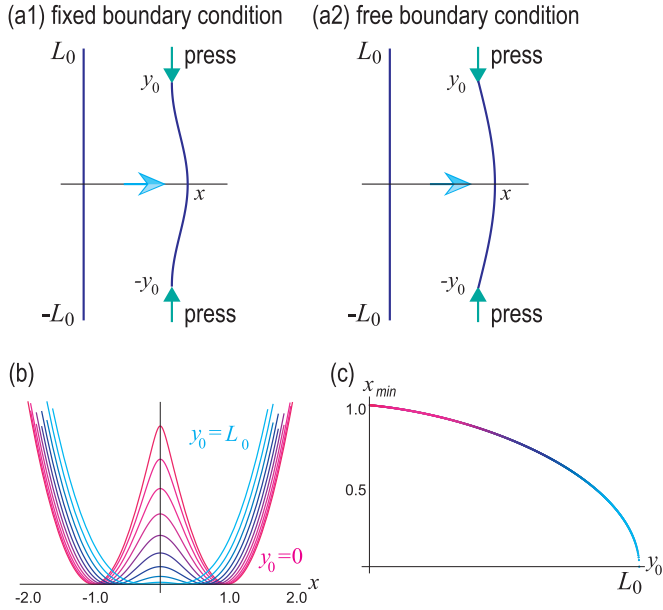
FIG. 12. Illustration of a buckled plate with (a1) fixed boundary condition and (a2) free boundary condition. (b) The potential $V(x)$ in Eq. (A7) for various y_0 as a function of x in units of x_u. (c) The potential minimum point $x_{\min}$ in units of x_u as a function of y_0.

where E is the complete elliptic integral of the second kind defined by

$$E(k) \equiv \int_0^{\pi/2} \sqrt{1 - k^2 \sin^2\theta} d\theta. \qquad (A6)$$

With the use of Eq. (A5), the potential energy is given by the Hooke law,

$$V(x) = \frac{\kappa}{2}[2L(x) - 2L_0]^2, \qquad (A7)$$

which we show for various y_0 in Fig. 12(b). It is a double-well potential. The point $x_{\min}$ at which the potential $V(x)$ takes the minimum is shown as a function of y_0 in Fig. 12(c).

We expand Eq. (A7) in x by fixing L_0 and y_0 as

$$V(x) = \frac{\kappa}{2}(2L_0 - 2y_0)^2 + \frac{1}{4y_0}(L_0 - y_0)\kappa\pi^2 x^2$$
$$+ \frac{(3y_0 - L_0)}{256 y_0^3}\kappa\pi^4 x^4 + o(x^6), \qquad (A8)$$

which is summarized as

$$V(x) = \lambda(x^2 - a^2)^2 + V_0 + o(x^6), \qquad (A9)$$

with

$$\lambda \equiv \frac{3y_0 - L_0}{256 y_0^3}\kappa\pi^4, \quad a \equiv y_0 \frac{4\sqrt{2}}{\pi}\sqrt{\frac{L_0 - y_0}{3L_0 - y_0}}. \qquad (A10)$$

By neglecting the terms V_0 and $o(x^6)$ in Eq. (A9), we obtain the double-well potential (1) in the main text under the fixed boundary condition.

Second, we impose the free boundary condition as shown in Fig. 12(a2), which reads

$$\left.\frac{d^2w}{dy^2}\right|_{x=-y_0} = \left.\frac{d^2w}{dy^2}\right|_{x=y_0} = 0, \qquad (A11)$$

whose solution is [51]

$$w = x_0 \cos\frac{\pi y}{2y_0}. \qquad (A12)$$

The length $L(x_0)$ is given by Eq. (A5) precisely as in the case of the fixed boundary condition. The potential energy is given by the same Hooke law as Eq. (A7). Hence, we also obtain the double-well potential (1) in the main text under the free boundary condition.

APPENDIX B: QUANTUM TUNNELING

Quantum tunneling between the two states $|0\rangle$ and $|1\rangle$ is estimated by means of the Wentzel-Kramers-Brillouin (WKB) approximation. The tunneling rate Γ is given by

$$\Gamma = e^{-2\varsigma}, \quad \varsigma \equiv \frac{1}{\hbar}\int_{-a}^{a} dx|\sqrt{2mV_{\text{DW}}(x)}|. \qquad (B1)$$

For the double-well potential (1), we find

$$\varsigma = \frac{\sqrt{2m\lambda}}{\hbar}\frac{4a^3}{3}. \qquad (B2)$$

Hence, the quantum tunneling is exponentially small as a function of a. a is estimated as

$$a \equiv y_0 \frac{4\sqrt{2}}{\pi}\sqrt{\frac{L_0 - y_0}{3L_0 - y_0}} = 0.127 \text{ μm}, \qquad (B3)$$

where we have used $L_0 = 1$ μm, $y_0 = 0.99$ μm. By using $m = 10^{-21}$ kg and $\lambda = 3 \times 10^{15}$ kg/m^2 s^2, the ς is estimated as

$$\varsigma = 3.1 \times 10^{10}. \qquad (B4)$$

Thus, the tunneling rate Γ is negligibly small.

APPENDIX C: COHERENCE TIME

In this Appendix, we derive [34–38] the formula (28) for the relaxation time T_1 and the coherence time T_2 used in Sec. IV. We consider a Hamiltonian system H_S coupled to an environment H_B via an interaction Hamiltonian H_{int}. The whole Hamiltonian is given by

$$H = H_S + H_B + H_{\text{int}}. \qquad (C1)$$

The environment Hamiltonian is given by

$$H_B = \sum_k \omega_k b_k^\dagger b_k, \qquad (C2)$$

while the interaction Hamiltonian is given by

$$H_{\text{int}} = L \otimes (B + B^\dagger) + L^\dagger \otimes (B + B^\dagger), \qquad (C3)$$

with

$$B = \sum_k g(k)b(k), \qquad (C4)$$

where L is the Lindbladian operator describing the dissipation mechanism, $b(k)$ is a bosonic operator, and $g(k)$ is the coupling constant between the system and the environment.

The Lindblad equation for the density matrix ρ reads

$$\frac{d\rho}{dt} = -\frac{i}{\hbar}[H_S, \rho] + \gamma_- \sum_j \left(L\rho L^\dagger - \frac{1}{2}\{L^\dagger L, \rho\}\right)$$
$$+ \gamma_+ \sum_j \left(L^\dagger \rho L - \frac{1}{2}\{LL^\dagger, \rho\}\right), \quad \text{(C5)}$$

where

$$\gamma_- = \gamma[\bar{n}_{\text{th}}(\omega_0) + 1], \quad \gamma_+ = \gamma\bar{n}_{\text{th}}(\omega_0), \quad \text{(C6)}$$

with the Bose distribution (29) and the decay rate γ. We consider a two-level system described by

$$H = \frac{\Omega}{2}\sigma_z, \quad L_- = \gamma_-\sigma_-, \quad L_+ = \gamma_+\sigma_+, \quad L_z = \gamma_z\sigma_z. \quad \text{(C7)}$$

Here, L_- and L_+ describe amplitude damping, where L_- describes the stimulated emission and L_+ describes the stimulated absorption. It is introduced by thermal fluctuation. On the other hand, L_z describes the dephasing. It is introduced by voltage fluctuation. The Lindblad equation reads

$$\frac{d\rho}{dt} = -\frac{i}{\hbar}\left[\frac{\Omega}{2}\sigma_z, \rho\right] + \gamma_- \sum_j \left(\sigma_-\rho\sigma_+ - \frac{1}{2}\{\sigma_+\sigma_-, \rho\}\right)$$
$$+ \gamma_+ \sum_j \left(\sigma_+\rho\sigma_- - \frac{1}{2}\{\sigma_-\sigma_+, \rho\}\right)$$
$$+ \gamma_z \sum_j (\sigma_z\rho\sigma_z - \rho), \quad \text{(C8)}$$

which is explicitly given by

$$\frac{d\rho_z}{dt} = -\bar{\gamma}(\rho_z - \rho_{z\infty}), \quad \text{(C9)}$$

$$\frac{d\rho_{01}}{dt} = \left(i\Omega - \frac{\bar{\gamma}}{2} - 2\gamma_z\right)\rho_{01}, \quad \text{(C10)}$$

$$\frac{d\rho_{10}}{dt} = \left(-i\Omega - \frac{\bar{\gamma}}{2} - 2\gamma_z\right)\rho_{10}, \quad \text{(C11)}$$

where we have defined

$$\bar{\gamma} = \gamma_+ + \gamma_- = \gamma(2\bar{n}_{\text{th}} + 1), \quad \rho_{z\infty} = \frac{\gamma_+ - \gamma_-}{\gamma_+ + \gamma_-}. \quad \text{(C12)}$$

The solutions are

$$\rho_x(t) = e^{-(\bar{\gamma}/2 + 2\gamma_z)t}[\rho_x(0)\cos\Omega t - \rho_y(0)\sin\Omega t], \quad \text{(C13)}$$

$$\rho_y(t) = e^{-(\bar{\gamma}/2 + 2\gamma_z)t}[\rho_x(0)\sin\Omega t - \rho_y(0)\cos\Omega t], \quad \text{(C14)}$$

$$\rho_z(t) = [\rho_z(0) - z_\infty]e^{-\bar{\gamma}t} + \rho_{z\infty}. \quad \text{(C15)}$$

The relaxation times T_1 and T_2 are estimated as

$$T_1 = 1/\bar{\gamma}, \quad T_2 = 2/(\bar{\gamma} + 4\gamma_z). \quad \text{(C16)}$$

First, we evaluate the thermal fluctuation effect. The Caldeira-Legget model leads to an effective equation of motion,

$$m\frac{d^2x}{dt^2} = -\kappa x - \mu\frac{dx}{dt}, \quad \text{(C17)}$$

with $\mu = 2m\gamma$, and κ is the spring constant. The γ represents the friction $\gamma \equiv \mu/2\sqrt{m\kappa}$ in this context. The characteristic frequency is $\omega_0 = \sqrt{\kappa/m}$. The Q factor is an experimentally observable quantity given by $Q = \sqrt{m\kappa}\mu = \omega_0/2\gamma$. Alternatively, the γ can be estimated from the Q factor as

$$\gamma = \omega_0/2Q. \quad \text{(C18)}$$

It follows from Eq. (C16) and this equation that

$$T_1 = \frac{T_2}{2} = \frac{1}{\gamma(2\bar{n}_{\text{th}} + 1)} = \frac{2Q}{\omega_0(2\bar{n}_{\text{th}} + 1)}, \quad \text{(C19)}$$

which is Eq. (28) in the main text.

As a typical mass and a typical characteristic frequency, let us use those of a carbon nanotube [39], where $m = 10^{-21}$ kg and $\omega_0 = 2\pi \times 327$ MHz. For $Q = 4 \times 10^3$, we have

$$\gamma = \frac{\omega_0}{2Q} = \frac{327\,\text{MHz}}{8 \times 10^3} = 40.9\,\text{kHz}. \quad \text{(C20)}$$

By using the Boltzmann constant $k_B = 1.38 \times 10^{-23}$ m^2 kg/s^2 K, we estimate $\hbar\omega_0/k_BT \simeq 0.113$ at $T = 20$ mK. With the use of the Bose distribution (29), we have $\bar{n}_{\text{th}} \simeq 8.36$. The relaxation time T_1 and the coherence time T_2 are estimated as

$$T_1 = \frac{T_2}{2} = \frac{1}{\gamma(2\bar{n}_{\text{th}} + 1)} = 1.38\,\mu\text{s}. \quad \text{(C21)}$$

For an ultrahigh quality factor $Q = 10^6$ as in Refs. [19,40–43], the decay rate is estimated as

$$\gamma = \frac{\omega_0}{2Q} = \frac{327\,\text{MHz}}{2 \times 10^6} = 163\,\text{Hz}. \quad \text{(C22)}$$

The relaxation time T_1 and the coherence time T_2 are estimated as

$$T_1 = \frac{T_2}{2} = \frac{1}{\gamma(2\bar{n}_{\text{th}} + 1)} = 0.346\,\text{ms}. \quad \text{(C23)}$$

These results are given in Eqs. (30) and (31) in the main text.

Next, we estimate the coherence time due to the dephasing. The main source of the voltage fluctuation is the Johnson-Nyquist noise, which is determined by

$$V_N = \sqrt{4k_BTR\Delta f}. \quad \text{(C24)}$$

The resistance ratio of the nanotube [52,53] is 2.5×10^{-3} Ωcm, which leads to the resistance $R = 2.5 \times 10^{-7}$ Ω for a nanotube with 1 μm length. By inserting $T = 20$ mK and $f_0 = 327$ MHz, we find $V_N = 9.5 \times 10^{-12}$ V. The energy for the voltage fluctuation is 0.95 μeV = 230 MHz. Then, the dephasing time is estimated as 4.3 μs.

Finally, we evaluate the operation time in order to estimate how many times it is possible to execute quantum gate operations. The spring constant is estimated as $\kappa = m\omega_0^2 = 4.22 \times 10^3$ kg/s^2. By assuming a length of a NEMS $L_0 = 1$ μm and the buckled length $y_0 = 0.99$ μm, we find

$$\lambda \equiv \frac{3y_0 - L_0}{256y_0^3}\kappa\pi^4 \simeq \frac{\kappa\pi^4}{128L_0^2} = 3 \times 10^{15}\,\text{kg/m}^2\,\text{s}^2. \quad \text{(C25)}$$

The unit operation time is estimated as $t_u = (m^2/\hbar\lambda)^{1/3} = 10$ ns. The typical gate time is $40t_u = 0.4$ μs, as shown in Fig. 4. It is possible to execute quantum gates 1.38 μs/0.4 μs $\simeq 3$ times for a sample with $Q = 4 \times 10^3$ and 10.5 μs/0.4 μs $\simeq 26$ times for a sample with $Q = 10^6$.

[1] R. Feynman, Simulating physics with computers, Intl. J. Theor. Phys. **21**, 467 (1982).

[2] D. P. DiVincenzo, Quantum computation, Science **270**, 255 (1995).

[3] M. Nielsen and I. Chuang, *Quantum Computation and Quantum Information* (Cambridge University Press, Cambridge, 2016).

[4] Y. Nakamura, Yu. A. Pashkin, and J. S. Tsai, Coherent control of macroscopic quantum states in a single-Cooper-pair box, Nature (London) **398**, 786 (1999).

[5] E. Knill, R. Laflamme and G. J. Milburn, A scheme for efficient quantum computation with linear optics, Nature (London) **409**, 46 (2001).

[6] D. Loss and D. P. DiVincenzo, Quantum computation with quantum dots, Phys. Rev. A **57**, 120 (1998).

[7] J. I. Cirac and P. Zoller, Quantum Computations with Cold Trapped Ions, Phys. Rev. Lett. **74**, 4091 (1995).

[8] L. M. K. Vandersypen, M. Steffen, G. Breyta, C. S. Yannoni, M. H. Sherwood, and I. L. Chuang, Experimental realization of Shor's quantum factoring algorithm using nuclear magnetic resonance, Nature (London) **414**, 883 (2001).

[9] B. E. Kane, A silicon-based nuclear spin quantum computer, Nature (London) **393**, 133 (1998).

[10] C. Psaroudaki and C. Panagopoulos, Skyrmion Qubits: A New Class of Quantum Logic Elements Based on Nanoscale Magnetization, Phys. Rev. Lett. **127**, 067201 (2021).

[11] J. Xia, X. Zhang, X. Liu, Y. Zhou, and M. Ezawa, Universal Quantum Computation Based on Nanoscale Skyrmion Helicity Qubits in Frustrated Magnets, Phys. Rev. Lett. **130**, 106701 (2023).

[12] J. Xia, X. Zhang, X. Liu, Y. Zhou, and M. Ezawa, Qubits based on merons in magnetic nanodisks, Commun. Mater. **3**, 88 (2022).

[13] Y. Mita, A. Hirakawa, B. Stefanelli, I. Mori, Y. Okamoto, S. Morishita, M. Kubota, E. Lebrasseur, and A. Kaiser, Progress and opportunities in high-voltage microactuator powering technology towards one-chip MEMS, Jpn. J. Appl. Phys. **57**, 04FA05 (2018).

[14] R. Reddy, K. Komeda, Y. Okamoto, E. Lebrasseur, A. Higo, and Y. Mita, A zero-power sensing MEMS shock sensor with a latch-reset mechanism for multi-threshold events monitoring, Sens. Actuators, A **295**, 1 (2019).

[15] H. Toshiyoshi, Electrostatic actuation, in *Comprehensive Microsystems*, edited by Y. B. Gianchandani, O. Tabata, and H. Zappe (Elsevier, Amsterdam, 2008), Vol. 2, pp. 1.

[16] H. G. Craighead, Nanoelectromechanical systems, Science **290**, 1532 (2000).

[17] K. L. Ekinci and M. L. Roukes, Nanoelectromechanical systems, Rev. Sci. Instrum. **76**, 061101 (2005).

[18] M. Blencowe, Quantum electromechanical systems, Phys. Rep. **395**, 159 (2004).

[19] M. Poot and H. S. J. van der Zant, Mechanical systems in the quantum regime, Phys. Rep. **511**, 273 (2012).

[20] O. Słowik, K. Orlowska, D. Kopiec, P. Janus, P. Grabiec, and T. Gotszalk, Quantum mechanical aspects in the MEMS/NEMS technology, Meas. Autom. Monit. **62**, 2450 (2016).

[21] S. Rips and M. J. Hartmann, Quantum Information Processing with Nanomechanical Qubits, Phys. Rev. Lett. **110**, 120503 (2013).

[22] S. Rips, I. Wilson-Rae, and M. J. Hartmann, Nonlinear nanomechanical resonators for quantum optoelectromechanics, Phys. Rev. A **89**, 013854 (2014).

[23] F. Pistolesi, A. N. Cleland, and A. Bachtold, Proposal for a Nanomechanical Qubit, Phys. Rev. X **11**, 031027 (2021).

[24] M. Ezawa, E. Lebrasseur, and Y. Mita, Ising machine based on bistable microelectromechanical systems, J. Phys. Soc. Jpn. **91**, 114601 (2022).

[25] M. Vangbo, An analytical analysis of a compressed bistable buckled beam, Sens. Actuators, A **69**, 212 (1998).

[26] V. Intaraprasonk and S. Fan, Nonvolatile bistable all-optical switch from mechanical buckling, Appl. Phys. Lett. **98**, 241104 (2011).

[27] J. Martinez-Rincon and Y. V. Pershin, Bistable nonvolatile elastic-membrane memcapacitor exhibiting a chaotic behavior, IEEE Trans. Electron Devices **58**, 1809 (2011).

[28] H. J. Korsch and M. Gluck, Computing quantum eigenvalues made easy, Eur. J. Phys. **23**, 413 (2002).

[29] Mathematica: Solving the eigenvalue problem for a double well potential using a 1D particle in a box as a basis set, https://mathematica.stackexchange.com/questions/187471/solving-the-eigenvalue-problem-for-a-double-well-potential-using-a-1d-particle-i (unpublished).

[30] D. Deutsch, Quantum theory, the Church-Turing principle and the universal quantum computer, Proc. R. Soc. A **400**, 97 (1985).

[31] C. M. Dawson and M. A. Nielsen, The Solovay-Kitaev algorithm, Quantum Inf. Comput. **6**, 81 (2006).

[32] N. Schuch and J. Seiwert, Natural two-qubit gate for quantum computation using the *XY* interaction, Phys. Rev. A **67**, 032301 (2003).

[33] Y. Makhlin, Nonlocal properties of two-qubit gates and mixed states and optimization of quantum computations, Quantum Inf. Proc. **1**, 243 (2002).

[34] C. W. Gardiner and P. Zoller, *Quantum Noise*, 3rd ed. (Springer, Berlin, 2004).

[35] U. Weiss, *Quantum Dissipative Systems*, 4th ed. (World Scientific, Singapore, 2012).

[36] H. W. Wiseman and G. J. Milburn, *Quantum Measurement and Control* (Cambridge University Press, Cambridge, 2009).

[37] J. Hauss, A. Fedorov, S. Andr, V. Brosco, C. Hutter, R. Kothari, S. Yeshwanth, A. Shnirman and G. Schön, Dissipation in circuit quantum electrodynamics: Lasing and cooling of a low-frequency oscillator, New J. Phys. **10**, 095018 (2008).

[38] H.-P. Breuer and F. Petruccione, *The Theory of Open Quantum Systems* (Oxford University Press, Oxford, UK).

[39] I. Khivrich, A. A. Clerk, and S. Ilani, Nanomechanical pump-probe measurements of insulating electronic states in a carbon nanotube, Nat. Nanotechnol. **14**, 161 (2019).

[40] A. Vinante, M. Bignotto, M. Bonaldi, M. Cerdonio, L. Conti, P. Falferi, N. Liguori, S. Longo, R. Mezzena, A. Ortolan *et al.*, Feedback Cooling of the Normal Modes of a Massive Electromechanical System to Submillikelvin Temperature, Phys. Rev. Lett. **101**, 033601 (2008).

[41] J. D. Thompson, B. M. Zwickl, A. M. Jayich, F. Marquardt, S. M. Girvin, and J. G. E. Harris, Strong dispersive coupling of a high-finesse cavity to a micromechanical membrane, Nature (London) **452**, 72 (2008).

[42] T. Rocheleau, T. Ndukum, C. Macklin, J. B. Hertzberg, A. A. Clerk, and K. C. Schwab, Preparation and detection of a

mechanical resonator near the ground state of motion, Nature (London) **463**, 72 (2010).

[43] C. Urgell, W. Yang, S. L. De Bonis, C. Samanta, M. J. Esplandiu, Q. Dong, Y. Jin, and A. Bachtold, Cooling and self-oscillation in a nanotube electromechanical resonator, Nat. Phys. **16**, 32 (2020).

[44] M. Despont, J. Brugger, U. Drechsler, U. Durig, W. Haberle, M. Lutwyche, H. Rothuizen, R. Stutz, R. Widmer, G. Binnig, H. Rohrer, and P. Vettiger, VLSI-NEMS chip for parallel AFM data storage, Sens. Actuators, A **80**, 100 (2000).

[45] C. A. Spindt, A thin-film field-emission cathode, J. Appl. Phys. **39**, 3504 (1968).

[46] C. Y. Maghfiroh, A. Arkundato, Misto, and W. Maulina, Parameters (σ, ϵ) of Lennard-Jones for Fe, Ni, Pb for potential and Cr based on melting point values using the molecular dynamics method of the LAMMPS program, IOP Conf. Ser.: J. Phys.: Conf. Ser. **1491**, 012022 (2020).

[47] H. Yamaguchi, S. Miyashita, and Y. Hirayama, Microelectromechanical displacement sensing using InAs/AlGaSb heterostructures, Appl. Phys. Lett. **82**, 394 (2003).

[48] M. Tortonese, H. Yamada, R. C. Barrett, and C. F. Quate, Atomic force microscopy using a piezoresistive cantilever (unpublished).

[49] T. Ando, High-speed atomic force microscopy and its future prospects, Biophys. Rev. **10**, 285 (2018)

[50] B. Charlot, W. Sun, K. Yamashita, H. Fujita, and H. Toshiyoshi, Bistable nanowire for micromechanical memory, J. Micromech. Microeng. **18**, 045005 (2008).

[51] T. N. Binh, S. Morishita, M. Kubota, and Y. Mita, A stiffness-defined silicon plane bending method to realize perfectly-curved surface formation for tunable parabolic mirrors, doi: 10.1109/omems.2012.6318802.

[52] T. W. Ebbesen, H. J. Lezec, H. Hiura, J. W. Bennett, H. F. Ghaemi, and T. Thio, Electrical conductivity of individual carbon nanotubes, Nature (London) **382**, 54 (1996).

[53] Y. Inoue, Y. Suzuki, Y. Minami, J. Muramatsu, Y. Shimamura, K. Suzuki, A. Ghemes, M. Okada, S. Sakakibara, H. Mimura, and K. Naito, Anisotropic carbon nanotube papers fabricated from multiwalled carbon nanotube webs, Carbon **49**, 2437 (2011).

[54] X. M. H. Huang, C. A. Zorman, M. Mehregany, and M. L. Roukes, Nanodevice motion at microwave frequencies, Nature (London) **421**, 496 (2003).

[55] N. E. Flowers-Jacobs, D. R. Schmidt, and K. W. Lehnert, Intrinsic Noise Properties of Atomic Point Contact Displacement Detectors, Phys. Rev. Lett. **98**, 096804 (2007).

[56] J. D. Teufel, J. W. Harlow, C. A. Regal, and K. W. Lehnert, Dynamical Backaction of Microwave Fields on a Nanomechanical Oscillator, Phys. Rev. Lett. **101**, 197203 (2008)

[57] G. Anetsberger, O. Arcizet, Q. P. Unterreithmeier, R. Riviere, A. Schliesser, E. M. Weig, J. P. Kotthaus, and T. J. Kippenberg, Near-field cavity optomechanics with nanomechanical oscillators, Nat. Phys. **5**, 909 (2009).

[58] M. Li, W. H. P. Pernice, and H. X. Tang, Broadband all-photonic transduction of nanocantilevers, Nat. Nanotechnol. **4**, 377 (2009).